Chinese Chemical Letters 37 (2026) 112296

Contents lists available at ScienceDirect

Chinese Chemical Letters

journal homepage: www.elsevier.com/locate/cclet

Unraveling crystalline-phase-effect of CoSe for highly efficient and robust Fenton-like catalysis: A combined experimental and theoretical study

Xianghan Cheng[a], Xiaoli Wang[a], Zhen Li[a,*], Ping Niu[a], Junjie Tian[a,c], Yong-Zheng Zhang[a], Da-Shuai Zhang[a], Xiuling Zhang[a], Weixuan Huang[d], Longlong Geng[a,*], Xing Xu[b,*]

[a] Shandong Provincial Key Laboratory of Monocrystalline Silicon Semiconductor Materials and Technology, College of Chemistry and Chemical Engineering, Dezhou University, Dezhou 253023, China
[b] School of Environmental Science and Engineering, Shandong University, Qingdao 266237, China
[c] Dezhou Green Chemical and Environmental Catalysis Engineering Research Center, Dezhou Luba Fine Chemical Co., Ltd., Dezhou 253023, China
[d] Faculty of Education and Liberal Arts, NTI International University, Persiaran Perdana BBN, Putra Nilai, 71800 Nilai, Negeri Sembilan, Malaysia

ARTICLE INFO

Article history:
Received 28 July 2025
Revised 12 October 2025
Accepted 17 December 2025
Available online 18 December 2025

Keywords:
Advanced oxidation process
Crystal phase engineering
CoSe nanocrystals
PMS activation
Tetracycline degradation

ABSTRACT

The development of novel catalysts with both robust activity and long-term stability is significant but remains a critical challenge for the degradation of emerging pollutants. Herein, CoSe nanocrystal-embedded amorphous carbon (CoSe/MC) was rationally designed and synthesized *via* an *in situ* selenization strategy. Interestingly, the unique hierarchical architecture featuring CoSe nanocrystal cores and carbon shells simultaneously exposes abundant accessible active sites and enhances stability during the Fenton-like process. Under ambient conditions, CoSe/MC achieves 97% tetracycline (TC) degradation within 2 min, with a rate constant of 3.74×10^{-2} s^{-1}, which is 7.3-fold faster than Co_3O_4/C. Furthermore, CoSe/MC exhibits remarkable versatility across a wide pH range (3–11), various water sources (*e.g.*, river/lake water), and diverse pollutants (*e.g.*, antibiotics/dyes). Continuous-flow tests confirm long-term stability (>95% efficiency over 300 min) with negligible metal leaching (<0.1 mg/L Co). Mechanistic studies reveal a synergistic radical/non-radical pathway dominated by $^1O_2$ generation, validated by EPR spectroscopy and quenching experiments. Density functional theory (DFT) calculations further elucidate the key role of CoSe in activating PMS by elongating O–O bonds considerably and accelerating electron transfer, which synergistically promotes O–O cleavage and the generation of reactive oxygen species during TC degradation.

© 2026 Published by Elsevier B.V. on behalf of Chinese Chemical Society and Institute of Materia Medica, Chinese Academy of Medical Sciences.

Emerging pollutants, such as antibiotics, endocrine disruptors, and persistent organic pollutants, pose significant threats to ecosystems and human health due to their biotoxicity, environmental persistence, and bioaccumulation potential [1]. For instance, antibiotics are resistant to degradation in aqueous environments and can readily promote the proliferation of drug-resistant bacteria, rendering them difficult to remove efficiently through conventional wastewater treatment methods [2,3]. Advanced oxidation processes (AOPs) based on permonosulfate (PMS) activation have demonstrated exceptional efficacy in mineralizing complex organic contaminants into CO_2 and H_2O, by generating highly reactive oxygen species (ROS), such as $SO_4^{\bullet-}$, $^{\bullet}OH$ and $^1O_2$, which possess high oxidation potentials and rapid reaction kinetics [4]. Furthermore, AOPs-PMS offer distinct advantages including operational simplicity and compatibility across a broad pH range, thereby avoiding the generation of iron sludge commonly associated with the traditional Fenton process.

In recent years, cobalt-based catalysts have come to the forefront as the most prominent research focus, primarily attributed to their remarkable ability to efficiently activate PMS [5,6]. At present, the majority of catalysts are plagued by issues such as inadequate exposure of active sites, low electron transport efficiency, or structural instability, which ultimately lead to a decline in PMS activation efficiency [7,8]. In response to these challenges, a diverse range of highly efficient cobalt oxide catalysts have been developed. These efforts involve strategies such as elemental doping, modulation of metal-support interactions, and the design of cluster and single-atom catalysts, all aimed at promoting the $Co^{2+} \leftrightarrow Co^{3+}$ redox cycling [9]. For instance, bimetallic catalysts like $CoFe_2O_4$ can

* Corresponding authors.
E-mail addresses: lizhendiyi@163.com (Z. Li), llgeng@dzu.edu.cn (L. Geng), xuxing@sdu.edu.cn (X. Xu).

https://doi.org/10.1016/j.cclet.2025.112296
1001-8417/© 2026 Published by Elsevier B.V. on behalf of Chinese Chemical Society and Institute of Materia Medica, Chinese Academy of Medical Sciences.

inhibit metal leaching through the synergistic effect between Fe and Co and enhance the generation of ROS. Nevertheless, further optimization of the support is still necessary to increase the specific surface area and the density of active sites. Moreover, cobalt-based metal-organic framework (MOF)-derived materials, such as Co@N–C, exhibit excellent degradation performance, owing to their porous structure and highly dispersed active sites [10]. Despite their great promise, cobalt oxides still encounter the problem of metal ion leaching under oxidative operating conditions. This not only results in secondary pollution but also leads to poor long-term cycling performance. Consequently, it is both urgent and crucial to bridge the gap between insufficient catalyst activity and suboptimal stability through rational catalyst design. Engineering the crystalline phase holds great potential to significantly enhance the efficiency and stability of metal-based catalysts [11,12].

Engineering the crystalline phase of metal-based materials holds the potential to significantly boost corresponding efficiency and stability during catalytic process [13]. This is achieved by precisely modulating the crystal structure, interfacial electronic states, and surface defects. Zhong *et al.* reported the successful optimization of the d-band center of cobalt in the $CoSe_2$/CoP heterojunction *via* crystal-amorphous interfacial coupling. This accomplishment led to a reduction in the kinetic potential barrier and remarkable improvement for hydrogen evolution reaction (HER) [14]. Yu and co-authors demonstrated that the distinctive structure of ultrafine $CoSe_2$ embedded onto N-doped porous carbon nanosheets ($CoSe_2$-NPCS) could expose an abundance of active sites and expedite electron transport. Consequently, it exhibited enhanced activity and structural stability in high-energy aluminum batteries [15]. These studies incontrovertibly reveal that the charge structure and chemical stability of Co-based catalysts can be effectively optimized through selenide engineering, which provides crucial design insights for the development of efficient and durable Co-based catalysts for AOPs [16].

In this study, through an innovative *in situ* selenization strategy, a novel hierarchically porous carbon-embedded CoSe nanocrystal catalyst (CoSe/MC) was successfully fabricated using a Co-MOF as precursor. Significantly, the selenization process facilitated the direct reaction between Co and Se, resulting in the formation of high-purity CoSe nanocrystals. Meanwhile, the thermally induced polycondensation of the MOF framework endowed the catalyst with a unique core (CoSe)-shell (amorphous carbon) architecture. Strikingly, the CoSe/MC exhibited superior PMS adsorption and activation capabilities, enabling the rapid removal of TC within 2 min, with a rate constant 7.3 times higher than that of Co_3O_4/C. Furthermore, CoSe/MC also demonstrated remarkable stability, maintaining full activity for over 300 min during continuous TC degradation process. A combination of DFT simulations and experimental analyses clarified the PMS activation and charge transfer pathways at the CoSe interface. Finally, the degradation pathways and mechanisms were systematically explored through quenching experiments, EPR spectroscopy, and intermediate identification.

The synthetic protocol for CoSe/MC is depicted schematically in Fig. 1a. The Co-MOF precursor was synthesized through a hydrothermal process involving coordination-driven self-assembly of Co^{2+} ions with terephthalate ligands. Through an innovative *in situ* phase engineering strategy, the CoSe/MC hybrid catalyst was synthesized by integrating controlled pyrolysis with gas-phase selenization. Figs. 1b-d present scanning electron microscopy (SEM) images of the synthesized materials. The parent Co-MOF precursor features well-defined rhombohedral microcrystals with smooth facets (Fig. 1b), which is characteristic of its high structural order. As illustrated in Figs. 1c and d, both the CoSe/MC and Co_3O_4/C preserve the parental morphology but exhibit evident surface roughness, which can be ascribed to the structural collapse induced by thermal treatment. The crystalline characteristics of the materials were systematically characterized using X-ray diffraction (XRD). The Co-MOF shows well-defined Bragg reflections in the range of 5°–50° (Fig. S1 in Supporting information), confirming its high crystallinity and phase purity. Elemental mapping of the CoSe/MC catalyst in Fig. 1e reveals a homogeneous distribution of Co, Se, and C elements throughout the sample, corroborating the excellent elemental dispersion. The microstructure of the CoSe/MC catalyst was further explored *via* high-resolution transmission electron microscopy (HRTEM). As depicted in Fig. 1f, the CoSe nanocrystals are encapsulated by amorphous carbon shells, forming a distinct core-shell architecture. This architecture is conducive to enhancing the stability of CoSe species during catalytic processes. The interlayer spacing of 0.264 nm measured in the HRTEM image corresponds to the (101) crystal plane of CoSe (Fig. 1g), while the interlayer spacing of 0.342 nm corresponds to amorphous carbon shells.

For CoSe/MC, three prominent diffraction peaks at $2\theta = 33.3°$, 44.8°, and 50.5° are respectively indexed to the (101), (102), and (110) crystallographic planes of hexagonal CoSe (JCPDS PDF #70–2870) [17]. In the XRD pattern of the Co_3O_4/C catalyst, the characteristic peaks positioned at 19.0°, 31.3°, 36.8°, and 44.8° are successfully identified as belonging to the Co_3O_4 phase (JCPDS PDF #42–1467), which is in accordance with previous reports (Fig. 2a) [18]. Figs. 2b and c present the N_2 adsorption–desorption isotherms and pore size distributions of the as-synthesized samples. As shown in Fig. 2b, both the Co-MOF and Co_3O_4/C exhibit relatively low adsorption capacities and hysteresis loops at $P/P_0 > 0.95$, which might be related to their stacking structures. Intriguingly, the CoSe/MC catalysts display type IV isotherms and H3 hysteresis loops between 0.55 and 0.95, indicating a mesoporous structure. The porous structure was further corroborated by the corresponding pore size distribution presented in Fig. 2b. In this figure, the pore size of the CoSe/MC predominantly falls within the range of 3–5 nm. Fig. 2c and Table S1 (Supporting information) comprehensively summarize the microstructural characteristics of various samples, encompassing the specific surface areas, pore volumes, and pore sizes. Specifically, the specific surface area and pore volume are 58.1 m^2/g and 0.18 cm^3/g for CoSe/MC, as opposed to 2.4 m^2/g and 0.021 cm^3/g for Co-MOF, and 5.4 m^2/g and 0.076 cm^3/g for Co_3O_4/C. For a solid catalyst, a larger specific surface area and higher porosity are advantageous as it can expose more catalytic active sites and facilitate catalytic conversion.

X-ray photoelectron spectroscopy (XPS) was utilized to analyze the surface chemistry and valence states of the elements in the Co-based catalysts [19]. The survey spectra of the catalysts presented in Fig. S2 (Supporting information) confirm the presence of C, Se, and Co on the surface of CoSe/MC, and C, O, and Co on the surface of Co_3O_4/C, respectively. This finding is in accordance with the EDS mapping results. The high-resolution Co 2p XPS spectra in Fig. 2d display characteristic peaks of Co $2p_{3/2}$ and Co $2p_{1/2}$ at 780 eV-781.8 eV and 795.1 eV-796.9 eV, respectively, for both catalysts [20,21]. Through split-peak fitting, the content ratio of Co^{2+} species was determined to be 73.8 % for CoSe/MC, which is notably higher than that of Co_3O_4/C (56.8 %). Moreover, compared to Co_3O_4/C, the binding energies of the peaks corresponding to Co^{2+} and Co^{3+} in the CoSe/MC catalysts exhibit a downward shift, indicating an increase in the charge density at the Co sites. This augmentation in charge density is beneficial for the efficient charge transfer during the catalytic process. The Se 3d XPS spectra of CoSe/MC are depicted in Fig. 2e. The characteristic peaks at 54.3 eV and 55.8 eV correspond to the Se $3d_{5/2}$ and Se $3d_{3/2}$ orbitals of Se^{2-}, respectively [22]. In the O 1s XPS spectra of Co_3O_4/C (Fig. 2f), the two characteristic peaks located at 529.8 eV and 531.5 eV can be ascribed to Co-O and -OH species, respectively [23,24].

The catalytic activities of CoSe/MC and Co_3O_4/C were initially evaluated by the degradation of tetracycline (TC) *via* PMS activation. As depicted in Fig. 3a, only limited TC degradation (47.8 % af-

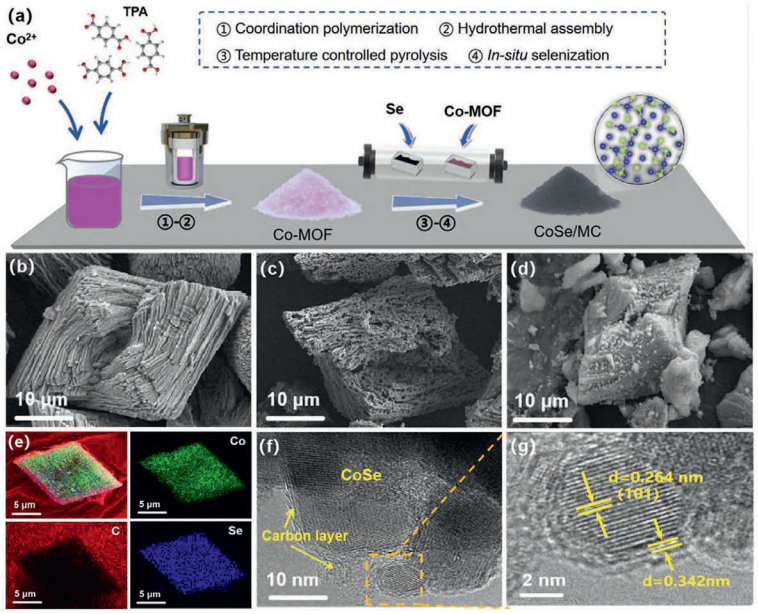


Fig. 1. (a) Schematic diagram of the synthesis procedure for CoSe/MC catalyst. SEM images of different Co-based catalysts (b) Co-MOF, (c) Co_3O_4/C and (d) CoSe/MC. (e) EDS mapping elements dispersion of CoSe/MC. (f) TEM image and (g) HRTEM image of CoSe/MC.

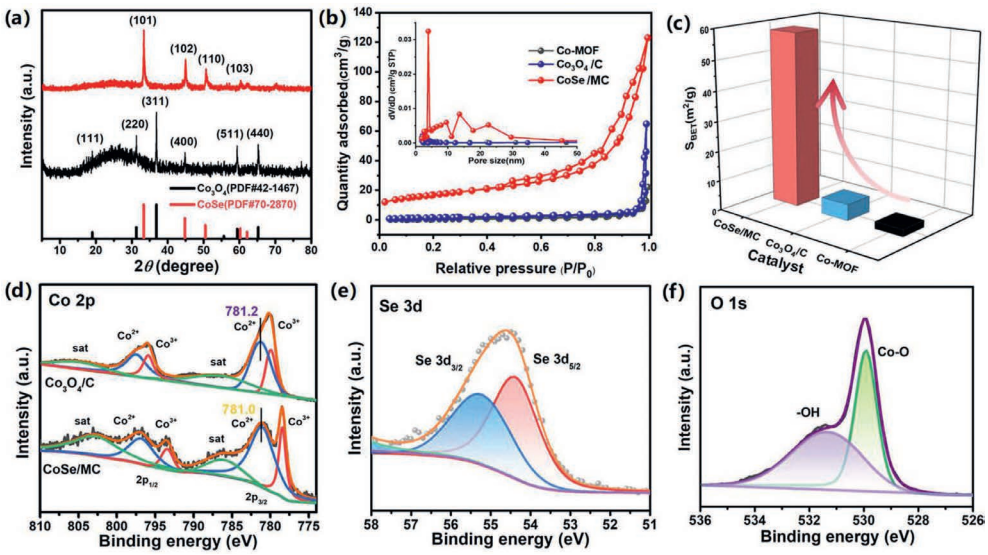


Fig. 2. (a) XRD pattern of CoSe/MC and Co_3O_4/C. (b) N_2 adsorption and desorption isotherms and (c) pore size distribution and specific area of Co-MOF, CoSe/MC and Co_3O_4/C, Co 2p. (d) High-resolution Co 2p spectrum of CoSe/MC and Co_3O_4/C. (e) Se 3d XPS spectra of CoSe/MC. (f) O 1s XPS spectra of Co_3O_4/C.

ter 10 min) was observed in the absence of any catalysts, which is consistent with previous studies [25]. The Co_3O_4/C/PMS system achieved TC removal rates of 48 % and 60 % at 2 min and 10 min, respectively. Especially for CoSe/MC/PMS system, the degradation efficiency of TC reached 97 % with a TOC value of 65.2 %, exhibiting superior activity under the same conditions. Notably, both catalysts exhibited moderate TC adsorption capacities, and CoSe/MC demonstrated a higher adsorption efficiency (37.9 % after 10 min) compared to Co_3O_4/C (10.1 %), which can likely be attributed to its mesoporous structure. A *pseudo*-first-order kinetic modeling was utilized to analyze the reaction kinetics of TC degradation over different catalysts (Fig. 3b). The apparent rate constant (k) of the CoSe/MC/PMS system reached $3.74 \times 10^{-2}\ s^{-1}$, which is 7.3 times higher than that of the Co_3O_4/C/PMS system ($0.514 \times 10^{-2}\ s^{-1}$). Notably, in terms of TC degradation efficiency and reaction time, the CoSe/MC/PMS system outperformed most of the previously reported Co-based catalysts (Fig. 3c and Table S2 in Supporting information), highlighting its practical application potential.

Subsequent investigations were carried out to evaluate the influence of reaction conditions on the catalytic activity of the CoSe/MC/PMS system. As illustrated in Figs. S3a-c (Supporting information), the results reveal that the degradation efficiency of TC increased significantly as the catalyst dosage was elevated from 0.06 g/L to 0.1 g/L. Nevertheless, beyond this concentration threshold, further increases in the catalyst dosage (>0.1 g/L) did not result in substantial enhancements in the degradation efficiency. A comparable trend was noted for the PMS concentration, where an excessive addition of the oxidant did not lead to a further improvement in the catalytic performance. As presented in Fig. 3d and Fig. S4 (Supporting information), the CoSe/MC/PMS system exhibited broad-spectrum degradation capabilities towards various pollutants, encompassing antibiotics and organic dyes. Specifically,

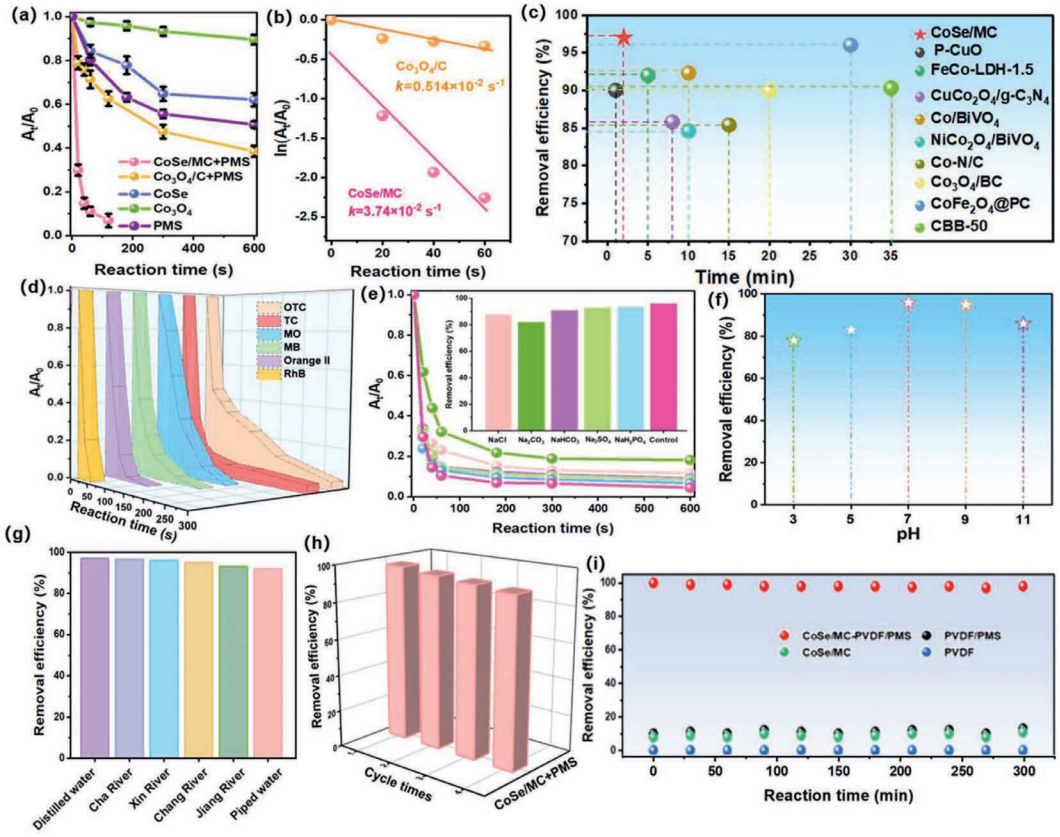


Fig. 3. (a) Degradation of TC over different catalytic systems and (b) the corresponding first-order kinetic reaction rate constants. (c) Comparison of degradation rate constant for pollutants degradation by PMS catalyzed in reported catalysts. (d) Effect of different pollutants, (e) influence of co-existing anions, (f) initial reaction pH and (g) water samples. (h) Stability of CoSe/MC/PMS and Co_3O_4/C/PMS for TC degradation. (i) Contaminant degradation performance of CoSe/MC - PVDF membranes.

more than 95 % degradation of organic dyes was accomplished within 3 min [26]. In contrast, antibiotics like pertussis antibiotic required longer treatment durations owing to their complex structures. Although coexisting anions and cations (*e.g.*, Na^+, Cl^-, SO_4^{2-}) generally impede the activation of PMS at the catalytic interfaces, the CoSe/MC/PMS system maintained an exceptional TC removal efficiency (>90 %) across diverse ionic environments (Fig. 3e), highlighting its robust resistance to interference. Moreover, the system sustained a TC degradation efficiency of over 85 % across a wide pH range (3–11), verifying its adaptability to fluctuating aqueous conditions (Fig. 3f). The activity of the CoSe/MC/PMS system was also evaluate using different water matrices, including deionized water and natural samples collected from rivers and lakes in Dezhou City. As depicted in Fig. 3g, a TC degradation efficiency of >90 % was consistently attained across all the tested matrices. This outstanding performance under environmentally relevant conditions underscores the robustness of CoSe/MC/PMS system against complex water components.

Apart from high catalytic activity, the stability and reusability are critical for a catalyst during practical applications. As depicted in Fig. 3h, CoSe/MC demonstrated a TC degradation efficiency surpassing 95 % over four consecutive cycles, highlighting its exceptional cycling stability. The XRD patterns obtained after the reaction showed no distinguishable alterations in peak positions or intensities (Fig. S5 in Supporting information), thereby confirming the structural integrity of the catalyst. This stability can be attributed to its distinctive core (CoSe)-shell (amorphous carbon) structure, which effectively alleviates the leaching of active species and phase transformations. Moreover, CoSe/MC displayed notable ferromagnetism (Fig. S6 in Supporting information). This property enables rapid magnetic recovery through external magnetic fields, while CoSe/MC maintains re-dispersibility upon the removal of the magnetic field.

To explore the usage potential of CoSe/MC in long-term applications, a CoSe/MC-PVDF membrane reactor was fabricated *via* vacuum filtration (Fig. S7 in Supporting information). As demonstrated in Fig. 3i, neither the pristine PVDF membrane nor the CoSe/MC-PVDF/PMS system (in the absence of PMS) exhibited significant TC removal. Notably, the CoSe/MC-PVDF/PMS system achieved complete elimination of TC (>95 %) during 300 min of continuous operation, with negligible cobalt leaching (<0.1 mg/L). This sustained performance emphasizes the feasibility of integrating CoSe/MC into flow-through configurations for industrial wastewater treatment.

To elucidate the reaction mechanism and identify the reactive oxygen species (ROS) involved in the CoSe/MC/PMS system, radical quenching experiments and electron paramagnetic resonance (EPR) spectroscopy were conducted [27–29]. According to previous reports, methanol (MeOH) and *tert*–butanol (TBA) were utilized to selectively scavenge sulfate radicals ($SO_4^{\bullet-}$) and hydroxyl ($^{\bullet}OH$) radicals, whereas *p*-benzoquinone (BQ) and L-histidine (L-His) were employed to specifically quench superoxide radicals ($O_2^{\bullet-}$) and singlet oxygen ($^1O_2$), respectively [30]. As shown in Fig. S8a (Supporting information), the corresponding contribution percentages of $^{\bullet}OH$, $O_2^{\bullet-}$, $SO_4^{\bullet-}$ and $^1O_2$ were recognized as 17.1 %, 21.2 %, 7.9 % and 53.8 %, respectively. These findings confirm the simultaneous occurrence of both radical pathways ($SO_4^{\bullet-}$, $^{\bullet}OH$, $O_2^{\bullet-}$) and non-radical pathways ($^1O_2$), with $^1O_2$ being the dominant ROS in PMS activation. EPR spectroscopy was further employed to directly detect the ROS generated in the CoSe/MC/PMS [31]. As illustrated in Figs. S8b-d (Supporting information), no EPR signals were ob-

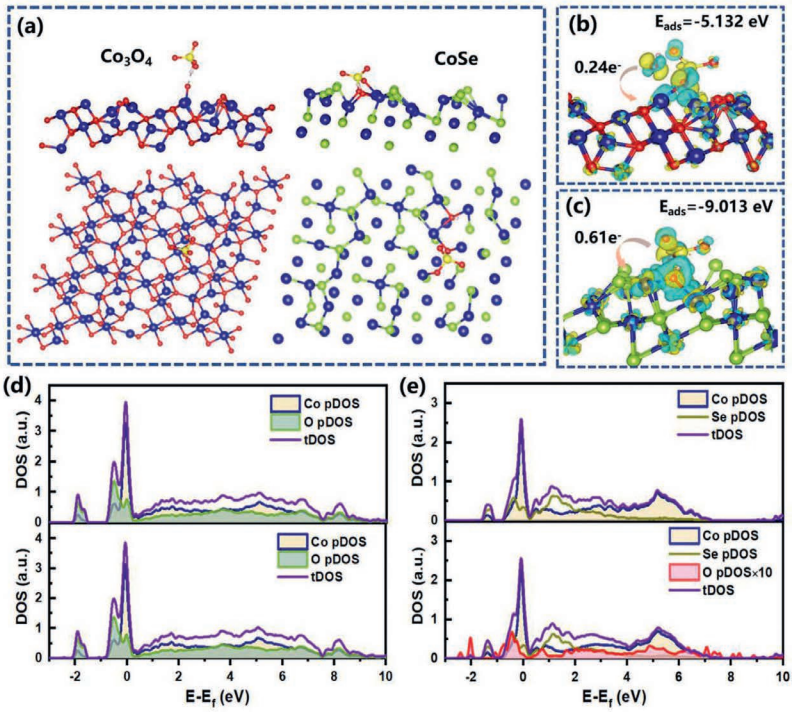


Fig. 4. (a) The optimized configurations of PMS adsorption on the Co_3O_4/C and CoSe/MC. Differences in charge densities of (b) Co_3O_4/C (c) and CoSe/MC (E_{ads}: surface adsorption energy). (d) Densities of states of O atoms adsorbed on Co_3O_4/C and (e) CoSe/MC in the optimal configurations (The electronic density of states is multiplied by 10 to facilitate clear analysis, since the amount of O in the system is very small).

served for CoSe/MC alone; however, distinct characteristic peaks corresponding to DMPO-$^{\bullet}$OH, DMPO-$SO_4^{\bullet-}$, DMPO–$O_2^{\bullet-}$, and TEMP-$^1O_2$ adducts appeared within 1 min after PMS addition. The signal intensities increased markedly after 3 min, clearly demonstrating that CoSe/MC effectively activates PMS to generate multiple ROS species.

Density functional theory (DFT) calculations were further performed to investigate the adsorption behavior and electronic interactions between PMS and Co sites on CoSe and Co_3O_4, and the optimized adsorption configurations were summarized in Fig. 4a [32,33]. Interestingly, PMS preferentially adsorbs onto Co_3O_4 through a "top" configuration, where the Co active site interacts with a single oxygen atom of PMS. In contrast, for CoSe, a "bridging" configuration is formed, in which the Co active site coordinates with two oxygen atoms of PMS. In addition, as shown in Figs. S9a and b (Supporting information), the O2-O3 bond length in free PMS is 1.48 Å. However, this value increases to 3.06 Å and 2.54 Å after being adsorbed on CoSe and Co_3O_4, respectively. This is consistent with the facilitated O–O cleavage and enhanced ROS generation during the TC degradation process [34,35]. The charge density difference of PMS adsorbed on CoSe and Co_3O_4 is depicted in Figs. 4b and c. Compared to the PMS-Co_3O_4 system, more apparent delocalization of charge was present at the interface of PMS and CoSe, indicating the stronger interactions and facilitated charge transfer between the reactant and catalyst. Bader charge analysis further confirms that more electron transfer (0.61 e^-) occurs between CoSe and PMS, which is significantly higher than that from Co_3O_4 (0.24 e^-), confirming its superior capability for PMS activation. The adsorption energy (ΔE_{ads}) of PMS on CoSe is −9.01 eV, which exceeds that on Co_3O_4 (−5.13 eV), indicating stronger chemisorption and enhanced capability in activating PMS. Density of states (DOS) analysis in Fig. 4d further emphasizes the multi-orbital coupling between Co atoms in CoSe and O atoms in PMS [36]. As for Co_3O_4, negligible changes are observed before and after PMS adsorption (Fig. 4e). Electrochemical impedance spectroscopy (EIS) was used to examine the charge transfer dynamics of different catalysts. The Nyquist plots in Fig. S10 (Supporting information)revealed a significantly smaller semicircle radius for CoSe/MC in comparison to Co_3O_4/C, indicating a marked reduction in charge transfer resistance and enhanced electrical conductivity [37].

Based on the results obtained from catalyst characterization, quenching experiments, and DFT calculations, a possible reaction mechanism for TC degradation in the CoSe/MC/PMS system was proposed. First, electron transfer takes place between Co^{2+} and PMS, activating PMS to generate $SO_4^{\bullet-}$ (Eq. 1) [38]. Concurrently, Co^{3+} is reduced to Co^{2+}, with the simultaneous formation of $SO_5^{\bullet-}$ (Eq. 2) [39]. The generated $SO_4^{\bullet-}$ then reacts with OH^- to produce $^{\bullet}$OH (Eq. 3). The formation of $O_2^{\bullet-}$ stems from the reaction of PMS in water to form H_2O_2. Subsequently, H_2O_2 further reacts with $^{\bullet}$OH to generate $HO_2^{\bullet}$, which ultimately leads to the formation of $O_2^{\bullet-}$ (Eqs. 4–6). The produced $O_2^{\bullet-}$ can rapidly react with H_2O to form $^1O_2$ (Eq. 7) [40]. Finally, the generated reactive oxygen species (ROS), including $^{\bullet}$OH, $SO_4^{\bullet-}$, $O_2^{\bullet-}$, and $^1O_2$, participate in the degradation of TC, yielding intermediates and eventually undergoing complete decomposition into carbon dioxide and water (Eq. 8) [41].

$$Co^{2+} + HSO_5^- \rightarrow Co^{3+} + SO_4^{\bullet-} + OH^- \quad (1)$$

$$Co^{3+} + HSO_5^- \rightarrow Co^{2+} + SO_5^{\bullet-} + H^+ \quad (2)$$

$$SO_4^{\bullet-} + OH^- \rightarrow {}^{\bullet}OH + SO_4^{2-} \quad (3)$$

$$HSO_5^- + H_2O \rightarrow H_2O_2 + HSO_4^- \quad (4)$$

$$HO^{\bullet} + H_2O_2 \rightarrow HO_2^{\bullet} + H_2O \quad (5)$$

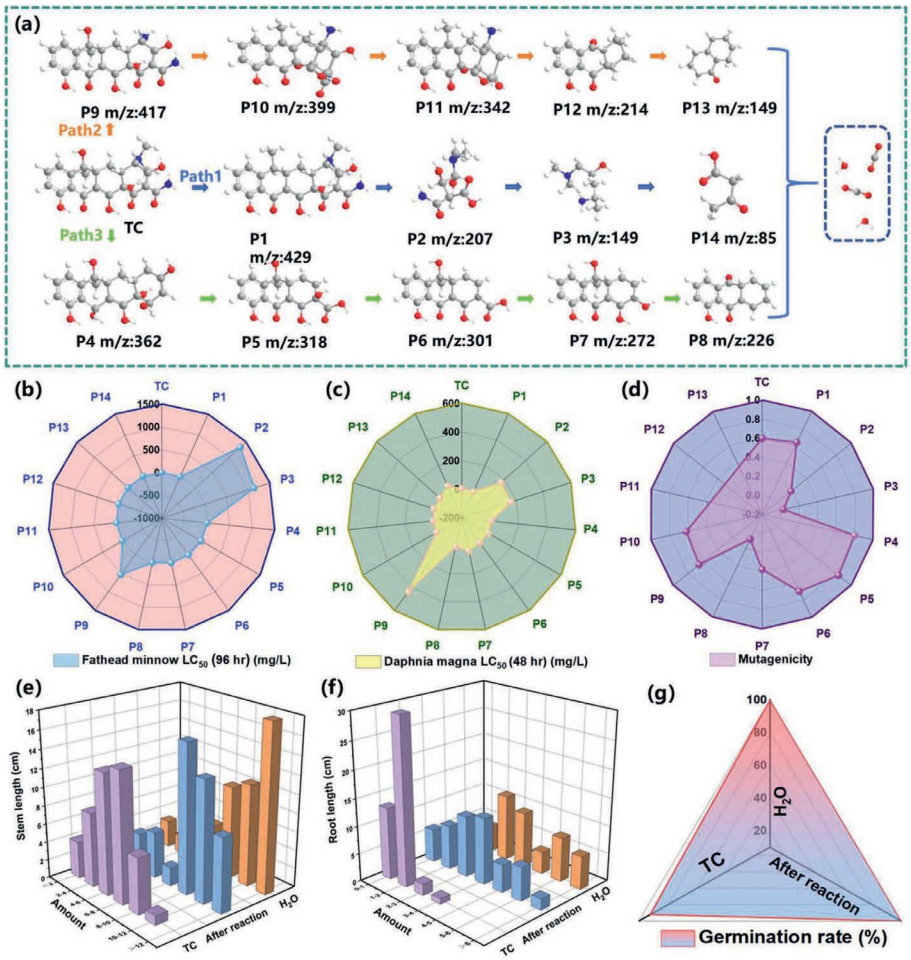


Fig. 5. (a) Proposed pathway of TC degradation by CoSe/MC/PMS system. (b) Fathead minnow LC_{50} (96 h), (c) daphnia magna LC_{50} (48 h), (d) mutagenicity of TC and other intermediates. (e) The germination rate, (f) root length and (g) stem length of 50 randomly selected mung beans in different solutions.

$$HO_2^{\bullet} \rightarrow H^+ + O_2^{\bullet -} \quad (6)$$

$$2O_2^{\bullet -} + 2H_2O \rightarrow 2^1O_2 + 2OH^- + H_2O_2 \quad (7)$$

$$TC + ROS \rightarrow \text{intermediates} \rightarrow CO_2 + H_2O \quad (8)$$

To elucidate the degradation pathways of TC in the CoSe/MC/PMS system, liquid chromatography-mass spectrometry (LC-MS) was employed to identify intermediate products [42–44]. As summarized in Fig. 5a and Table S3 (Supporting information), fourteen intermediates with *m/z* values ranging from 85 to 429 were detected, including **P1** (*m/z* 429), **P2** (*m/z* 207), **P3** (*m/z* 149), and others. Based on the LC-MS data and previous literature, three primary degradation pathways were proposed: (1) TC undergoes dehydration to form **P1** (*m/z* 429), followed by demethylation to yield **P9** (*m/z* 417); (2) reactive oxygen species ($^{\bullet}OH$, $SO_4^{\bullet -}$, $O_2^{\bullet -}$, $^1O_2$) initiate phenolic ring cleavage *via* terminal oxidation, generating intermediates (*m/z* 207–399) through deamidation, carbonylation, and demethylation; and (3) the fragmented intermediates undergo complete mineralization of fragmented intermediates (*e.g.*, *m/z* 85) into CO_2 and H_2O, demonstrating the system's synergistic radical- and non-radical-mediated oxidation capacity for efficient antibiotic elimination.

The environmental and biological impacts of TC and its degradation intermediates were assessed using acute toxicity tests (96-h LC_{50} for *Pimephales promelas*) and bioaccumulation potential evaluations (for *Daphnia magna*). Generally, lower LC_{50} and IC_{50} values indicate a higher toxicity of the intermediate. As depicted in Figs. 5b and c, predictions conducted using the Toxicity Estimation Software Tool (T.E.S.T.) revealed that most intermediates exhibited significantly reduced acute toxicity compared to the parent TC, with the exception of a few byproducts that could not be predicted [36,45–47]. In addition, mutagenicity assays in Fig. 5d also confirmed non-mutagenic properties for the majority of the detected intermediates. These findings, combined with minimal bioaccumulation risks, highlight the environmental compatibility of the CoSe/MC/PMS system and support its potential for sustainable antibiotic wastewater remediation.

Additionally, the phytotoxicity of TC and its degradation products was assessed using mung bean germination assays [48]. As shown in Figs. S11a and b (Supporting information), morphological analysis indicated near-identical growth patterns in TC-degraded solutions and ultrapure water controls, with only minor differences in developmental kinetics. In contrast, from Fig. S11c (Supporting information) shows that undegraded TC exhibited significant inhibition of both seed germination and seedling growth, even at low concentrations. Figs. 5e-g summarized the quantitative evaluation results including germination rates, measurements of root and stem lengths after seven days. Germination rates reached 100 % in ultra-pure water and degraded solutions, but declined to 92 % in TC solution. This inhibitory trend was further evident in seedling development: roots and stems in TC solution averaged 1–2 cm and 4–8 cm, respectively, compared to 2–4 cm (roots) and 8–12 cm

(stems) in control and degraded solutions. These results demonstrate effective biotoxicity elimination of TC through degradation, confirming the ecological safety of the CoSe/MC/PMS system for treating antibiotic-contaminated wastewater.

In summary, a novel CoSe/MC catalyst featuring a unique CoSe core and amorphous carbon shell was designed and synthesized using an *in situ* selenization strategy. This strategy has been engineered to activate PMS rapidly and degrade antibiotics efficiently. The optimized CoSe/MC achieves 97 % removal of TC within 2 min, with a rate constant 7.3-fold higher than that of Co_3O_4/C. Additionally, CoSe/MC exhibits remarkable adaptability across a broad pH range (3–11) and tolerance to coexisting ions. Continuous-flow operation confirms long-term stability (>95 % efficiency over 300 min) with negligible leaching of Co (<0.1 mg/L), while magnetic recovery ensures practical reusability. Toxicity assessments highlight reduced acute toxicity and non-mutagenic intermediates. Mechanistic studies reveal a synergistic degradation pathway involving both radical ($SO_4^{\bullet-}$, $^{\bullet}OH$, $O_2^{\bullet-}$) and non-radical ($^1O_2$) pathways, where $^1O_2$ dominates due to optimized interfacial charge redistribution, as evidenced by DFT calculations and EPR analysis. This study not only advances the rational design of durable PMS activators through crystalline phase engineering but also provides a sustainable solution for antibiotic-contaminated wastewater remediation.

CRediT authorship contribution statement

Xianghan Cheng: Writing – original draft, Investigation, Formal analysis. **Xiaoli Wang:** Software, Formal analysis. **Zhen Li:** Writing – original draft, Formal analysis. **Ping Niu:** Formal analysis. **Junjie Tian:** Investigation, Formal analysis. **Yong-Zheng Zhang:** Methodology, Formal analysis. **Da-Shuai Zhang:** Software, Investigation. **Xiuling Zhang:** Visualization, Methodology. **Weixuan Huang:** Writing – review & editing. **Longlong Geng:** Writing – review & editing, Visualization, Methodology, Formal analysis. **Xing Xu:** Writing – review & editing, Visualization, Conceptualization.

Declaration of competing interest

The authors declare that they have no known competing financial interests or personal relationships that could have appeared to influence the work reported in this paper.

Acknowledgments

This work was financially supported by the National Natural Science Foundation of China (Nos. 52170086, 21902022), Qingchuang Science and Technology Plan of Shandong Province (Nos. 2021KJ054, DZUQC202303) and Qingchuang Talents Induction Program of Shandong Higher Education Institution, the Natural Science Foundation of Shandong Province (Nos. ZR20250C51, ZR2025MS138, ZR2018LB018), Science and Technology Plan of Dezhou University (Nos. 2023XKZX005, HXKT2024117, and 202511A0053) and Shandong Provincial Key Laboratory of Monocrystalline Silicon Semiconductor Materials and Technology (No. 2025KFKT020).

Supplementary materials

Supplementary material associated with this article can be found, in the online version, at doi:10.1016/j.cclet.2025.112296.

References

[1] M.K. Shahid, A. Kashif, A. Fuwad, Y. Choi, Coord. Chem. Rev. 442 (2021) 213993.
[2] B. Jing, Q. Zhang, M. Liu, et al., Appl. Catal. B: Environ. Energy 369 (2025) 125149.
[3] J. Yang, S. Tian, Z. Song, et al., Coord. Chem. Rev. 523 (2025) 216257.
[4] Y. Wang, Y. Liu, H. Zhang, et al., Chem. Soc. Rev. 54 (2025) 2436–2482.
[5] H. Deng, N. Zhao, J. You, et al., Chin. Chem. Lett. 36 (2025) 110650.
[6] H. Zhao, W. Qi, X. Tan, et al., Chin. Chem. Lett. 36 (2025) 110898.
[7] L. Geng, W. Zhou, X. Wang, et al., J. Alloys Compd. 888 (2021) 161494.
[8] L. Geng, Q. Zhang, X. Wang, et al., Appl. Catal. B: Environ. Energy 343 (2024) 123575.
[9] T. Ni, H. Zhang, L. Zhou, et al., Chin. Chem. Lett. 36 (2025) 110659.
[10] C. Wang, H. Yuan, F. Yu, et al., Chin. Chem. Lett. 34 (2023) 107128.
[11] H. Hu, D. Zhang, H. Liu, et al., Chin. Chem. Lett. 32 (2021) 557–560.
[12] Y. Jin, Z. Zhou, H. Han, Chin. J. Struct. Chem. 44 (2025) 100660.
[13] L. Geng, H. Liu, W. Zhou, et al., Chin. Chem. Lett. 35 (2024) 109120.
[14] S. Shen, Z. Wang, Z. Lin, et al., Adv. Mater. 34 (2022) 2110631.
[15] L. Yao, S. Ju, T. Xu, X. Yu, ACS Nano 15 (2021) 13662–13673.
[16] Z. Wang, M. Zhang, J. Wang, et al., Environ. Sci. Technol. 59 (2025) 7389–7398.
[17] Y. Jiang, M. Xie, F. Wu, et al., Small 17 (2021) 2102893.
[18] X. Cheng, Y. Liu, M. Yang, et al., Sep. Purif. Technol. 354 (2025) 129251.
[19] Y. Xu, Z. An, Y. Tang, Sci. China Chem. 68 (2025) 2867–2891.
[20] Z. Gao, H. Wang, J. Zhu, et al., Chem. Eng. J. 506 (2025) 159831.
[21] X. Zhang, N. Wang, L. Geng, et al., J. Colloid Interface Sci. 512 (2018) 844–852.
[22] M. Fu, H. Yu, R. Lv, et al., Small 20 (2024) 2312151.
[23] Z. Wang, G. Lv, C. Zhang, X. Sun, J. Clean. Prod. 341 (2022) 130881.
[24] W. Huang, X. Jin, Q. Li, et al., ACS Appl. Nano Mater. 6 (2023) 12497–12506.
[25] M. Yang, Y. Lu, W. Zhang, et al., J. Environ. Chem. Eng. 12 (2024) 114999.
[26] S.K. Chang, Q.U.A. Abbasi, Z. Abbasi, et al., Arab. J. Chem. 17 (2024) 105422.
[27] Z. Ouyang, C. Yang, J. He, et al., Chem. Eng. J. 402 (2020) 126122.
[28] C. Chen, Y. Jia, J. Liu, et al., Chem. Eng. J. 507 (2025) 160865.
[29] L. Ma, S. Liu, J. Xu, et al., J. Environ. Manag. 391 (2025) 126674.
[30] X. Cheng, Z. Liu, R. Wang, et al., J. Environ. Chem. Eng. 13 (2025) 117328.
[31] S. Jing, H. Li, H. Liang, et al., Chem. Eng. J. 516 (2025) 163118.
[32] X. Song, S. Diao, W. He, et al., Sep. Purif. Technol. 333 (2024) 125927.
[33] X. Liang, D. Wang, Z. Zhao, et al., Adv. Funct. Mater. 32 (2022) 2203001.
[34] M. Yang, X. Cheng, F. Geng, et al., J. Mater. Chem. A 13 (2025) 4329–4342.
[35] L. Geng, F. Geng, X. Cheng, et al., Chem. Eng. J. 500 (2024) 156731.
[36] X. Cao, Y. Liu, T. Feng, X. Huang, W. Qiu, J. Water Process. Eng. 71 (2025) 107383.
[37] J. Moses, N.T. Bharanitharan, T. Selvam, et al., Small Methods 9 (2025) 2500028.
[38] R. Ma, G. Zhou, M. Gu, et al., Appl. Surf. Sci. 648 (2024) 158980.
[39] Z. He, M. Chen, M. Xu, et al., Appl. Catal. B: Environ. Energy 335 (2023) 122883.
[40] Y. Yu, N. Li, X. Lu, et al., J. Hazard. Mater. 421 (2022) 126735.
[41] X. Dong, X. Duan, Z. Sun, et al., Appl. Catal. B: Environ. Energy 261 (2020) 118214.
[42] M. Yu, C. Yang, M. Chen, et al., J. Hazard. Mater. 476 (2024) 135036.
[43] W. Wang, F. Song, C. Du, Y. Su, J. Colloid Interface Sci. 625 (2022) 479–492.
[44] Z. He, Y. He, F. Chang, et al., Chemosphere 286 (2022) 131759.
[45] J. Li, X. Tang, X. Guo, et al., J. Environ. Chem. Eng. 12 (2024) 114734.
[46] H. Wang, Z. Long, R. Chen, et al., Sep. Purif. Technol. 331 (2024) 125598.
[47] Y. Li, T. Song, C. Wang, et al., Chem. Eng. J. 507 (2025) 160499.
[48] W.W. Hong, X.H. Chen, X.D. Xiao, et al., Appl. Surf. Sci. 690 (2025) 162603.